
Article:
Ye, C., Yang, J., Xiong, F. et al. (1 more author) (2019) Relationship between homopolar inductor machine and wound-field synchronous machine. IEEE Transactions on Industrial Electronics. ISSN 0278-0046

https://doi.org/10.1109/tie.2019.2898577

Relationship between Homopolar Inductor Machine and Wound-field Synchronous Machine

C. Ye, J. Yang, F. Xiong, Z.Q. Zhu

***Abstract*—The homopolar inductor machine (HIM) has attracted recent interest in the field of flywheel energy storage system due to its merits of high-speed operation and low idling losses. In some situations, the analytical methods of a conventional wound-field synchronous machine (WSM) can be used to analyze the HIM, but the clear explanation about why these can be done and the relationship between HIM and WSM were not given in literature. To address these issues, this paper studies the HIM based on the basic theoretical model and equations. Firstly, the structure and magnetic circuit characteristics of HIM are introduced. Secondly, the mathematical model of HIM is derived and then decomposed, which indicates that the HIM can be seen as a WSM with large end leakage inductance when rotor tooth width $\theta_t \leq \pi/\mathrm{p}$, or consisting of a WSM and a synchronous reluctance machine (SRM) when $\theta_t > \pi/p$. Thirdly, the performances of HIM and corresponding machines, including air-gap flux density distribution, back electromotive force and inductance parameters, are analyzed and fully compared. Finally, an HIM is prototyped and tested on an experimental platform. The simulation and experiment results show that it is reasonable to regard the HIM as a WSM or a combination of WSM and SRM. The conclusions can be applied in the simplification of the design and analysis of HIM.**

***Index Terms*--Equivalent method, homopolar inductor machine (HIM), wound-field synchronous machine (WSM).**

NOMENCLATURE

E_0	No-load back electromotive force (back-EMF).
U	Terminal voltage of HIM.
I, I_d, I_q	Current of armature winding and its *d*- and *q*-axis components.
X_d, X_q	Reactances of *d*- and *q*-axes.
r_a	Resistance of armature winding.
μ_0	Airgap permeability.
g_1, g_2	Maximum and minimum lengths of air-gap.
p	Number of pole pairs.
m, n, ν	Number of harmonics.
θ	Position along the inside of stator relative to the *a*-phase axis.
θ_r	Angle between rotor frame *d*-axis and *a*-phase axis.
N_s	Total number of turns for each phase.
$I_f, I_{f,l}$	Field current of HIM and equivalent model (EM).
$N_f, N_{f,l}$	Number of turns per coil of HIM and EM field winding.
a, b, c	Name of phases.
k_{Nm}	Winding factor corresponding to m_{th} harmonic.
ϕ_L, ϕ_R	Fluxes on the left and right side of field winding.
w	Parallel branch numbers for each armature winding.
F_j	MMF generated by phase-*j*.
i_j	Current of phase-*j*.
$\Lambda_{sL}(\theta)$	Permeance function of the left air-gap of EM.
$\Lambda_{sR}(\theta)$	Permeance function of the right air-gap of EM.

I. INTRODUCTION

As one of the popular energy storage technologies, flywheel energy storage system (FESS) has the merits of high power density, large number of charge-discharge cycles, fast response time, pollution-free [1], [2]. It has been widely employed in the fields of transportation, power grid, military, aerospace, and so on [3]

In the FESS, an electrical machine is essentially indispensable to convert the kinetic energy to electrical energy, and vice versa. The most widely used is permanent magnet (PM) synchronous machine for its simple structure and high operation efficiency [4]. However, the PM machine would suffer from continuous free-wheeling losses caused by the stator core loss and rotor eddy current loss. Though the efficiency of PM machine is high, the idling losses would be a part of the total energy storage and result in a high self-discharge rate, especially in a long-term standby state [5]. To reduce the idling losses of PM machines, the coreless stators and Halbach configurations are adopted [6]. The power density of those PM machines would be reduced due to the increase of equivalent air-gap length. Besides, the complexity and cost of those PM machines would increase. The electrical machines without PMs can effectively suppress the idling losses. For the high-speed induction machine, the solid rotor topology is usually preferred due to its mechanical robustness [7]. It has the merits of simple and high strength rotor structure and high circumferential speed. While the solid rotor structure lacks bars that provide high conductivity for the rotor induced current, which results in the relatively low efficiency. To reduce the loss on the rotor, the methods including the axial slitting of solid-rotor [8], coating the solid rotor with a copper layer [9], or the rotor made of laminated high-strength sheet steels [10] are used. These methods could effectively reduce the eddy current loss of rotor. However, they would reduce the mechanical strength of rotor or the power factor, as well as increase the complexity of rotor structure [11]. For the switched reluctance machine, the simple construction and the ability to operate in the harsh operational environments make it suitable for the applications of the air blowers and the starter/generator system for the more-electric aircraft engine [12]. Due to its own vibration and noise, it is rarely used in the field of flywheel energy storage at present. For the wound-rotor synchronous and synchronous reluctance machines without PMs, they would suffer from some

drawbacks such as low reliability of brushes and flux bridges at high rotational speed respectively, low tip speed resulting from vulnerable rotor strength, and thus, low power densities. Of the various electrical machine topologies, homopolar inductor machines (HIMs) have attracted attentions and have been applied to the FESS in recent years [13], [14]. Because the magnetizing flux of HIM is generated by field windings, the excitation current could be switched off in the free-wheeling operation state, and thus the idling losses would be reduced. In spite of the relatively lower torque density than that of the PM machines, HIMs are able to offer favorable merits of the simple and robust rotor structure, brushless exciting and low idling losses [15]. Hence, HIMs can significantly reduce long-term high-speed operation self-discharge losses, which is essential for the FESS.

To facilitate the theoretical analysis of HIM, some investigations have been carried out. The HIM features unipolar magnetizing air-gap flux density, which can be discomposed into a series of ac components and a dc component. The rotor teeth and slots are respectively corresponding to the different polarity of fundamental air-gap flux density, which is dissimilar with that of the conventional wound-field synchronous machine (WSM) [16]. It caused the discussions about the definition of the HIM *d*- and *q*- axes and whether the two-reaction theory is applicable to this machine. In response to this issue, Erdelyi and Siegl claimed that the two-reaction theory cannot be suitable for the HIM because this machine has only the *d*-axis [17], [18]. After that, the numerical method is used to analyze the HIM under load condition, which is complex and time consuming. And thus it is not convenient for the practical application. Then, Lorilla [19], Tsao [13] and Tajima [20] derived the mathematical model based on the Park transformation to analyze the HIM. They used the two-reaction theory to calculate the armature reaction inductance, but it was not proved whether the two-reaction theory can be applicable to this type of machine. To address this flaw, Lou et al. certified that the two-reaction theory was applicable to HIM by finite element analysis (FEA) method and experiments, and thus pointed out that the design and analysis method of HIM could refer to that of the WSM, while the relationship between the HIM and WSM was not illustrated [16], [21]. Severson et al. derived the electromagnetic torque of bearingless HIM according to the torque equation of conventional synchronous machine, and then obtained that the electromagnetic torque of HIM concludes the reluctance and alignment torque [22]. Hence, the HIM can be seen as consisting of a synchronous reluctance motor and a cylindrical synchronous motor. The model of the synchronous reluctance motor has been provided according to the effective air-gap. Unfortunately, the structure of cylindrical synchronous motor cannot be obtained according to this paper. Yang et al. proposed a simplified 2-D analytical model, WSM, of HIM with the rotor tooth width $\theta_t \leq \pi/\mathrm{p}$ based on the spatial overlay method to reduce the time to calculate the effective magnetizing air-gap flux density of HIM [23]. This model only considers the effective magnetizing air-gap flux density relationship between the 2-D equivalent model and HIM. Other relationships between HIM and WSM have not been studied. At the same time, some articles describe the HIM as much like a WSM [24]. The main difference between them is that the excitation winding of WSM is on the rotor and that of the HIM is on the stator, and there is no clear and in-depth explanation.

As can be seen from the summary of previous investigations, some analysis methods of WSM have been used to analyze the HIM. However, a clear explanation about the relationship between WSM and HIM is not given and needs more in-depth investigations, which will be the focus of this paper. This paper is organized as follows. In Section II, the topology and operation principle of HIM are introduced. In Section III, the expressions of the key parameters of HIM are derived, including the air-gap flux density, back-EMF and inductances. In Section IV, the mathematical model of HIM is derived and the equivalent model (EM) of HIM is proposed. In Section V, results obtained from the EM are compared with those of 3-D FEA and corresponding experiments.

II. Machine Topology and Operation Principle

The structure of dual-segment-core HIM is shown in Fig.1 (a). Its rotor is made of solid steel. Both ends of the rotor have same number of rotor teeth. The left and right rotor tooth axes are differed by π electrical degree from each other. The HIM has two stator cores, which are both made of laminated silicon steel laminations. A concentrated field winding is sandwiched by the two stator sections and encircles the rotor. A conventional three-phase armature winding is embedded in the two stators along the axial direction. A stator sleeve is made of solid steel, which encloses the rotor and stator and channels the homopolar magnetizing flux generated by the field winding.

When excitation current is injected into the field winding, the 3-D homopolar magnetizing flux of HIM is generated, as shown in Fig. 1(b). One end of the rotor core is magnetized as South-pole and the other is magnetized as North-pole. The air-gap permeance corresponding to the rotor teeth and slots are different, which contributes to the air-gap flux density to be not equal in the circumferential direction. Hence, the back-EMF would be generated when the rotor rotates.

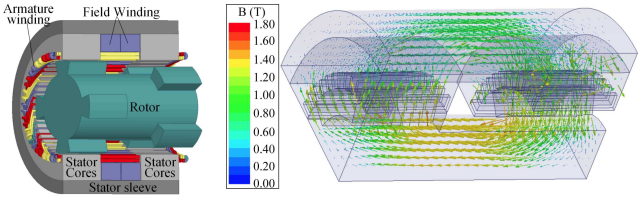

Fig. 1. HIM. (a) Structure. (b) Magnetizing flux.

III. Mathematical Model of HIM

In this section, the mathematical model of HIM is derived. The assumptions are made as follows: i) The iron of HIM has infinite permeability, and hence the saturation of iron cores is neglected; ii) Flux only crosses the air-gap radially. iii) The HIM works in a steady state.

A. Function of air-gap permeance

The radial cross-section of the HIM on one side of field winding is shown in Fig. 2, where γ is the ratio of the rotor tooth width θ_t to the slot pitch $2\pi/p$, as described by

$$\gamma = \theta_t/(2\pi/p) \tag{1}$$

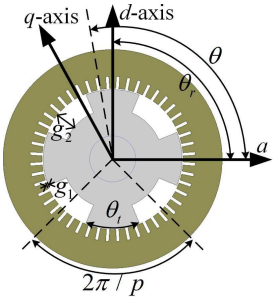

Fig. 2 Radial cross-section of the HIM on one side of field winding.

The maximum and minimum permeances per unit area of air-gap can be expressed as

$$\Lambda_{\max} = \mu_0/g_1\ ;\ \Lambda_{\min} = \mu_0/g_2\ . \tag{2}$$

Hence, the permeance function for the air-gap on the left side of field winding is

$$\Lambda_L(\theta-\theta_r) = \sum_{m=0}^{\infty} a_m \cos[mp(\theta-\theta_r)] \quad m=0,\ 1,\ 2,\ 3\cdots. \tag{3}$$

where

$$a_0 = \mu_0[1/g_2 + \gamma(1/g_1 - 1/g_2)] \tag{4}$$

$$a_q = (2\mu_0/\pi)(1/g_1 - 1/g_2)\sin q\gamma\pi \quad q=1,\ 2\ ,\ 3\cdots. \tag{5}$$

The salient iron poles on both sides of excitation winding differ π electrical degree from each other. Therefore, the permeance function for the air-gap on the right side of field winding can be calculated by

$$\Lambda_R(\theta-\theta_r) = \sum_{m=0}^{\infty} a_m \cos[mp(\theta\text{-}\theta_r\text{-}\pi/p)]. \tag{6}$$

B. No-load back-EMF

The magnetomotive force (MMF) generated by the field winding acts upon the left and right air-gaps in opposite direction. It can be expressed as

$$F_R\text{=-}F_L = N_f i_f/2. \tag{7}$$

The air-gap flux on both sides of field winding is depicted in Fig. 3, which shows that the directions of magnetizing flux in the left and right air-gaps under a coil of armature winding are opposite. Besides, the fluxes on both sides of field winding under the same coil are not equal due to the rotor tooth and slot.

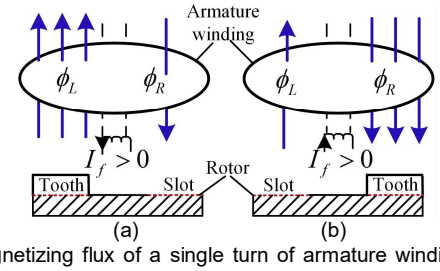

Fig. 3. Magnetizing flux of a single turn of armature winding on both sides of field winding. (a) The rotor tooth corresponding to the coil is on the left side of field winding. (b) The rotor tooth corresponding to the coil is on the right side of field winding.

The air-gap flux density waveforms on both sides of field winding are respectively depicted in Figs. 4(a), (c) and (e) when $\theta_t < \pi/4, \theta_t = \pi/4$, and $\theta_t > \pi/4$. The left and right air-gap flux densities can be decomposed into a series of harmonics, as described by

$$B_L = F_L\Lambda_L(\theta-\theta_r) = (N_f i_f/2)\sum_{m=0}^{\infty} a_m \cos[mp(\theta-\theta_r)] \tag{8}$$

$$B_R = F_R\Lambda_R(\theta-\theta_r) = -(N_f i_f/2)\sum_{m=0}^{\infty} a_m \cos[mp(\theta\text{-}\theta_r\text{-}\pi/p)] \tag{9}$$

The flux linkages generated by the field winding that links a single turn of an armature winding, which spans π electrical degree, can be calculated as

$$\begin{aligned}\phi_{j.f} &= \int_{h\frac{2\pi}{3p}-\frac{\pi}{2p}}^{h\frac{2\pi}{3p}+\frac{\pi}{2p}} (B_{L,f} + B_{R,f}) rld\theta \\ &= \int_{h\frac{2\pi}{3p}-\frac{\pi}{2p}}^{h\frac{2\pi}{3p}+\frac{\pi}{2p}} rlN_f i_f \sum_{m=2n+1}^{\infty} a_m \cos[mp(\theta-\theta_r)]\, d\theta.\end{aligned} \tag{10}$$

where h=0 when j=a, h=1 when j=b and h=2 when j=c.

(10) indicates that only the odd harmonics of air-gap flux density generated by the field winding would link with the armature winding. Besides, the odd harmonic components are the result of the spatial overlay of air-gap flux density on both sides of the field winding along the axial direction, which can be calculated as $B_L + B_R$. When the rotor tooth width $\theta_t < \pi/4, \theta_t = \pi/4$, and $\theta_t > \pi/4$, the waveforms obtained by spatial overlay method are respectively shown in Figs. 4(b), (d) and (f). As shown, the amplitude of those waveforms is $B_{max} - B_{min}$ and the resultant air-gap flux density is bipolar. In addition, the width of the waveform amplitude is θ_t when $\theta_t \leq \pi/4$. While the width of the waveform amplitude is $(2\pi/p - \theta_t)$ when $\theta_t > \pi/4$, which indicates that the amplitude width of effective air-gap flux density decreases with the increase of the rotor tooth width θ_t.

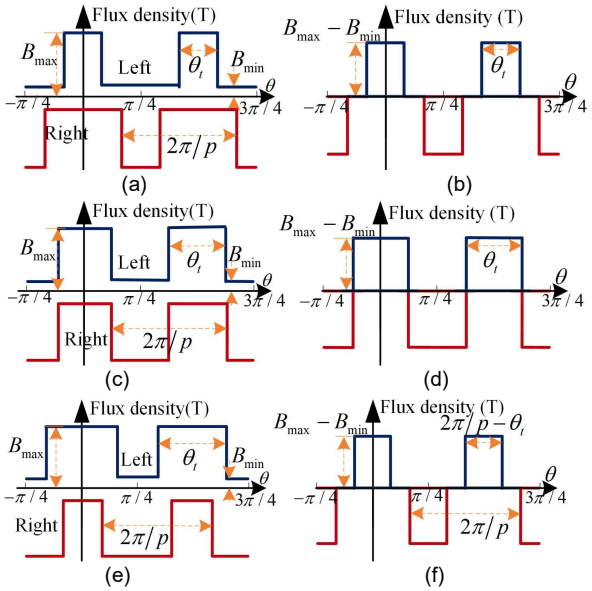

Fig. 4. Air-gap flux density distribution. (a), (c) and (e) respectively depict the flux density distribution on both sides of field winding when $\theta_t < \pi/4, \theta_t = \pi/4$, and $\theta_t > \pi/4$. (b), (d) and (f) are the flux density distribution obtained by the spatial overlay method when $\theta_t < \pi/4, \theta_t =$

$\pi/4$, and $\theta_t > \pi/4$, respectively.

The flux linkage per phase generated by the field winding current corresponding to each harmonic is given by

$$\lambda_{j,fm} = \frac{N_s}{w} k_{Nm} \int_{h\frac{2\pi}{3p}-\frac{\pi}{2p}}^{h\frac{2\pi}{3p}+\frac{\pi}{2p}} rlN_f i_f a_m \cos[mp(\theta-\theta_r)]d\theta. \quad (11)$$

Hence, the phase back-EMF of HIM can be calculated by

$$E_{j,m} = d\lambda_{j,fm}/dt. \quad (12)$$

C. Self- and mutual inductances of armature winding

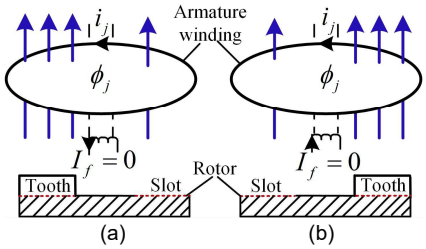

Fig. 5. Flux generated by armature winding on both sides of field winding. (a) The rotor tooth corresponding to the coil is on the left side of field winding. (b) The rotor tooth corresponding to the coil is on the right side of field winding.

The directions of flux generated by the armature windings on both sides of the field winding are the same, as shown in Fig. 5. The air-gap flux densities on the left and right sides of field winding can be respectively calculated by

$$B_{jL} = F_j \Lambda_L(\theta-\theta_r) = F_j \sum_{m=0}^{\infty} a_m \cos mp(\theta-\theta_r) \quad (13)$$

$$B_{jR} = F_j \Lambda_R(\theta-\theta_r) = F_j \sum_{m=0}^{\infty} a_m \cos mp(\theta-\theta_r-\pi/p). \quad (14)$$

The flux produced by the phase-*j* winding that links a single turn of phase-*k* winding can be calculated as

$$\begin{aligned}\phi_{k.j\nu} &= \int_{h\frac{2\pi}{3p}-\frac{\pi}{2p}}^{h\frac{2\pi}{3p}+\frac{\pi}{2p}} (B_{jL}+B_{jR}) rld\theta \\ &= \int_{h\frac{2\pi}{3p}-\frac{\pi}{2p}}^{h\frac{2\pi}{3p}+\frac{\pi}{2p}} F_j \Lambda_{2n}\, d\theta.\end{aligned} \quad (15)$$

where $k = a,\ b$ or c; $\Lambda_{2n} = \sum_{m=2n}^{\infty} 2a_m \cos[mp(\theta-\theta_r)]$, which is the sum of the left and right air-gap permeance.

Thus, the flux linkages of armature winding corresponding to ν_{th} harmonics generated by the armature winding are given by

$$\lambda_{k,j\nu} = (N_s/w) k_{Nm} \phi_{k,j\nu} \quad (16)$$

The inductance of armature winding is

$$L_{k,j\nu} = \lambda_{k,j\nu}/i_j \quad (17)$$

Therefore, the self- and mutual inductances of armature windings can be respectively expressed as

$$L_{j,j} = L_{ls} + \sum_{\nu=0}^{\infty} (\lambda_{j,j\nu}/i_j) \quad (18)$$

$$L_{k,j} = \sum_{\nu=0}^{\infty} (\lambda_{k,j\nu}/i_j) \quad (19)$$

According to (13)-(17), $L_{j,j}$ and $L_{k,j}$ depend to the rotor shape and are related to Λ_{2n}; L_{ls} is the leakage inductance of armature winding, which is equal to $L_{ls,end} + L_{ls,cores} + L_{ls,mid}$, as shown in Fig. 6(a).

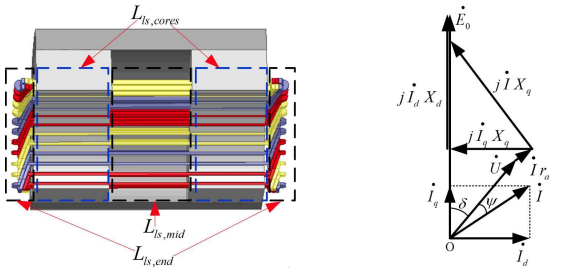

Fig. 6. (a) The leakage inductance distribution of armature winding, where $L_{ls,end}$, $L_{ls,cores}$ and $L_{ls,mid}$ are the end leakage inductance of armature winding, armature winding embedded in the stator slots and armature winding between two stator cores, respectively. (b) Phasor diagram for a single phase of HIM (generator convention).

IV. Equivalent Model

Based on the above derivations, the HIM can be transformed into another topology of machine, which is designated as an equivalent machine (EM). The specific processes are introduced as follows.

A. Electromotive force balance equation

The phasor diagram for a single phase of HIM is shown in Fig. 6(b). The electromotive force balance equation (generator convention) of HIM can be expressed as [16], [19]

$$\dot{E}_0 = \dot{U} + \dot{I} r_a + j\dot{I}_d X_d + j\dot{I}_q X_q \quad (20)$$

which indicates that if the parameters $\dot{E}_0$, X_d, X_q and r_a of a machine are equal to those of HIM, the output performances of HIM can be obtained by analyzing this machine.

B. Stator and armature winding

The stator structure and armature winding of EM are the same with those of HIM, as shown in Fig. 6(a). Hence, their leakage inductances $L_{ls,end}$ and $L_{ls,cores}$ of armature winding are equal, respectively.

C. Rotor

According to (20), the EM should meet the following two conditions. i) The magnetizing air-gap flux density of the EM is equal to the effective air-gap flux density of HIM, which ensures that the no-load back-EMF of the two machines are the same. ii) The air-gap permanence of the EM need to be equal to that of the HIM Λ_{2n}, which can ensure that the self- and mutual inductances of the armature windings of the two machines are equal. According to the effective air-gap flux density obtained by the spatial overlay method in Section III, the rotor structure of EM is divided into three types based on the tooth width θ_t of the HIM.

Case 1: $\theta_t < \pi/4$.

Fig. 7(a) shows the rotor structure of the HIM when $\theta_t < \pi/4$. Figs. 7(b) and (c) show the permeance waveforms of the left and right air-gaps of the HIM respectively. The air-gap permeance Λ_{2n} of HIM is shown in Fig. 9(a). According to the analysis in Section III, it can be found that the amplitude and

amplitude width of the effective air-gap flux density waveform of the HIM are θ_t and $(B_{max}-B_{min})$ respectively. To obtain the same effective magnetizing air-gap flux density of the HIM, the rotor structure of EM is given in Fig. 8(a), where the tooth width is θ_t and the maximum and minimum air-gap lengths are g_2 and g_1, respectively. It can be seen as translating the right section salient iron poles to the left section salient iron poles, and the rest of HIM rotor remains unchanged. Besides, salient poles with two different colours are magnetized to 'N' pole and 'S' pole, respectively. The amplitude of the air-gap flux density of EM is

$$B_{amp}=F_{EM}(\mu_0/g_1) \tag{21}$$

where F_{EM} is the air-gap MMF generated by the field winding of EM, which will be explored later. B_{amp} should equal to $(B_{max}-B_{min})$.

The permeance waveform of the left section of the EM is shown in Fig. 8(b). To make the permeance related to the self- and mutual inductance of armature winding of EM is Λ_{2n}, the permeance of right section of EM is

$$\Lambda_{sR(\theta_t<\pi/4)}(\theta-\theta_r)=\Lambda_{2n}(\theta-\theta_r)-\Lambda_{sL(\theta_t<\pi/4)}(\theta-\theta_r)=\mu_0/g_2 \tag{22}$$

which is depicted in Fig. 8(c). Hence, the air-gap length of right section of EM is g_2.

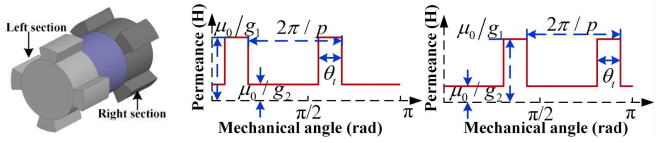

Fig. 7. Rotor of the HIM when $\theta_t<\pi/4$. (a) Structure. (b) and (c) is the airgap permeance on the left and right sections, respectively.

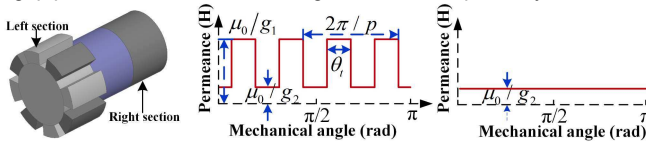

Fig. 8. Rotor of the EM when $\theta_t<\pi/4$. (a) Structure. (b) and (c) are the airgap permeance of the left and right sections, respectively.

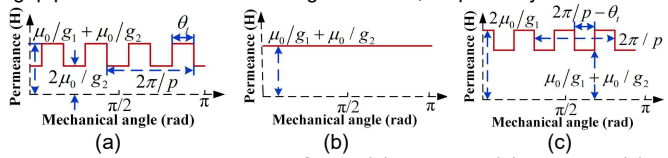

Fig. 9. Total air-gap permeance of HIM. (a) $\theta_t<\pi/4$. (b) $\theta_t=\pi/4$. (c) $\theta_t>\pi/4$.

Case 2: $\theta_t=\pi/4$.

The rotor structure of HIM with $\theta_t=\pi/4$ is shown in Fig. 10(a). Figs. 10(b) and (c) show the permeance waveforms of the left and right air-gaps of HIM, respectively. The corresponding air-gap permeance Λ_{2n} is shown in Fig. 9(b). As previous investigations, the amplitude and amplitude width of effective air-gap flux density are $(B_{max}-B_{min})$ and $\pi/4$, respectively. To obtain the same effective magnetizing air-gap flux density and air-gap permeance with those of the HIM, the corresponding rotor structure of the EM is shown in Fig. 11(a).

Rotor structure transformation process of case 2 is the same as the case 1. It can be found that the left and right sections of EM rotor are smooth. The air-gap lengths of the left and right sections are g_1 and g_2, respectively. The amplitude of air-gap flux density of the left section can be calculated by (21).

Figs. 11(b) and (c) respectively show the air-gap permeance waveforms corresponding to the left and right stator cores of EM. They meet the following equation

$$\Lambda_{sR(\theta_t=\pi/4)}(\theta-\theta_r)+\Lambda_{sL(\theta_t=\pi/4)}(\theta-\theta_r)=\Lambda_{2n}(\theta-\theta_r). \tag{23}$$

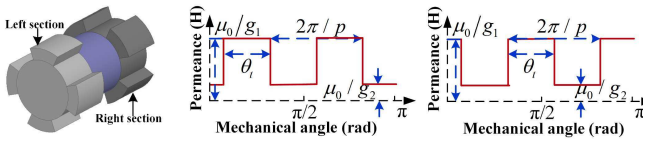

Fig. 10. Rotor of HIM when $\theta_t=\pi/4$. (a) Structure. (b) and (c) are the air-gap permeance of the left and right air-gaps, respectively.

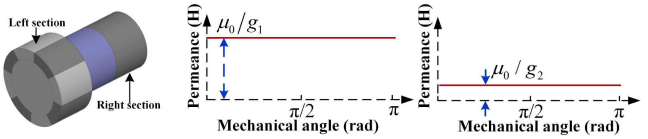

Fig. 11. Rotor of EM when $\theta_t=\pi/4$. (a) Structure. (b) and (c) are the air-gap permeance of the left and right air-gaps, respectively.

Case 3: $\theta_t>\pi/4$.

Fig. 12(a) shows the rotor structure of HIM with rotor tooth width $\theta_t>\pi/4$. It can be found that the rotor teeth of the left and right sections are partially overlap in the axial direction. The air-gap permeance waveforms of the left and right sections are depicted in Figs. 12(b) and (c), respectively. And the corresponding air-gap permeance Λ_{2n} is given in Fig. 9 (c). According to the study in Section Ⅲ, the amplitude and amplitude width of effective air-gap flux density of HIM are $(B_{max}-B_{min})$ and $(2\pi/p-\theta_t)$, respectively. To obtain the same effective air-gap flux density distribution with the HIM, the tooth width of rotor on the left section of EM is $(2\pi/p-\theta_t)$, as shown in Fig. 13(a). Its maximum and minimum air-gap lengths are g_2 and g_1, respectively. Adjacent rotor teeth are magnetized to different polarities. The amplitude of the air-gap flux density generated by the field winding of EM is also can be calculated by (21), which should equal to $(B_{max}-B_{min})$.

The permeance waveform of the left section of EM is shown in Fig. 13(b). To keep the air-gap permeance function of EM same as the HIM, the air-gap permeance of the right section of EM can be calculated as

$$\Lambda_{sR(\theta>\pi/4)}(\theta-\theta_r)=\Lambda_{2n(\theta>\pi/4)}(\theta-\theta_r)-\Lambda_{sL(\theta>\pi/4)}(\theta-\theta_r). \tag{24}$$

Its waveform is shown in Fig. 13(c). The tooth width of rotor on the right section is $(\theta_t-\pi/p)$. Its maximum and minimum air-gap lengths are g_2 and $g_1g_2/(2g_2-g_1)$, respectively.

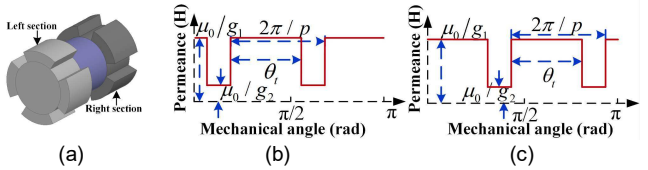

Fig. 12. Rotor of HIM when $\theta_t > \pi/4$. (a) Structure. (b) and (c) are the air-gap permeance of the left and right air-gaps, respectively.

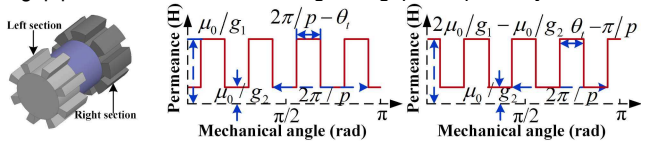

(a) (b) (c)

Fig. 13. Rotor of EM when $\theta_t > \pi/4$. (a) Structure. (b) and (c) are the air-gap permeance of the left and right air-gaps, respectively.

According to (22) to (24), it can be found that the air-gap permeances related to self- and mutual reluctances of the EM armature winding are equal to those of HIM. In addition, they have the same stator structure and armature winding. Hence, the self- and mutual inductances of the EM corresponding to the left and right rotor sections are the same with those of HIM. Meanwhile, the path of magnetic flux generated by the armature winding between two stator cores is unchanged. The leakage inductance $L_{ls,mid}$ of EM is the same with that of HIM. Hence, the self- and mutual inductances of the EM armature winding are the same as those of the HIM armature winding.

D. Field winding

To obtain the same armature winding flux linkages generated by the field winding of EM with those of the HIM, $2p$ sets of field windings are set on the left section of EM rotor, as shown in Fig. 14. For the rotor tooth width $\theta_t < \pi/4$ or $\theta_t > \pi/4$, each of rotor tooth encircles a field winding. For the rotor tooth width $\theta_t = \pi/4$, the field windings are uniformly placed on the rotor surface in the circumferential direction. Besides, the directions of field current between two adjacent windings are opposite. The number of turns of each excitation coil $N_{f,l}$ of the EM is half of that of the HIM excitation winding. The detailed progress for calculation the field current of EM was given in [23], which can be expressed as

$$I_{f,l} = I_f[(B_{\max} - B_{\min})/B_{\max}] \tag{25}$$

$$F_{EM} = N_{f,l} I_{f,l} \tag{26}$$

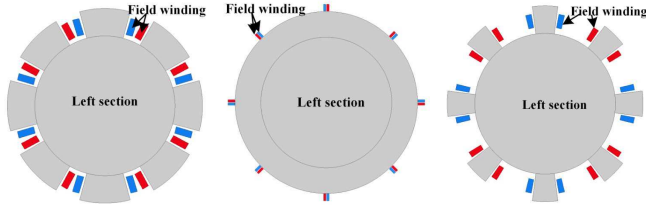

(a) (b) (c)

Fig .14. Section view of EM rotor. (a) $\theta_t < \pi/4$. (b) $\theta_t = \pi/4$. (c) $\theta_t > \pi/4$.

E. Structure of EM

Figs. 15(a), (b) and (c) show the structures of EM when $\theta_t < \pi/4$, $\theta_t = \pi/4$ and $\theta_t > \pi/4$, respectively. As shown, the structure of EM can be divided into three parts along the axial direction. It can be found that Part 1 is actually a conventional wound-field synchronous machine and Part 2 can be seen as the end-winding leakage inductance of WSM. When $\theta_t \le \pi/4$, Part 3 can be seen as the end-winding leakage inductance of WSM. Hence, the HIM with rotor tooth width $\theta_t \le \pi/4$ can be considered as a WSM with large end leakage inductance, and the torque of this machine is only created on the left rotor section. When $\theta_t > \pi/4$, Part 3 is the synchronous reluctance machine. Thus, the HIM with rotor tooth width $\theta_t > \pi/4$ can be seen as consisting of a WSM and a synchronous reluctance machine (SRM), and the torque is generated jointly by the left and right rotor sections.

According to the topologies of EM, it can be seen that when $\theta_t < \pi/4$, the synchronous reactance $x_d > x_q$; when $\theta_t = \pi/4$, $x_d = x_q$; and when $\theta_t > \pi/4$, $x_d < x_q$. Besides, the width of the effective air-gap flux density waveforms of HIM is equal to the rotor tooth width when $\theta_t \le \pi/4$. While when $\theta_t > \pi/4$, the width of effective air-gap flux density of HIM would decease with the increase of rotor tooth width due to the superposition of left and right magnetizing air-gap flux density. The flux per pole would increase as the tooth width increases, which results in lower flux utilization and the saturation of rotor and shell along the axial direction. Hence, $\theta_t \le \pi/4$ is a better choice for the rotor tooth width than $\theta_t > \pi/4$.

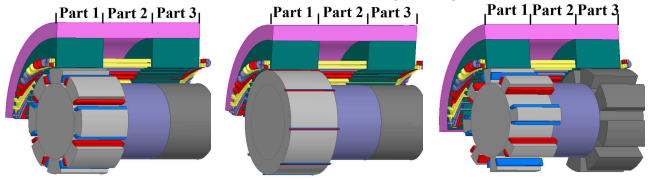

(a) (b) (c)

Fig. 15. Structures of EM. (a) $\theta_t < \pi/4$.(b) $\theta_t = \pi/4$. (c). $\theta_t > \pi/4$.

V. Simulation and Experimental Verification

To validate the effectiveness of the EM, the FEA method is implemented through the Maxwell software. The EM rotor is made of solid steel, which is same with that of the HIM. The HIMs with different rotor tooth width $\theta_t = \pi/6$ and $\theta_t = \pi/3$ are simulated as cases to validate the above analyses, whose parameters are shown in Table I.

TABLE I
HIM Key Parameters

Stator outer diameter(mm)	380
Stator inner diameter(mm)	245
Number of stator slots(--)	48
poles	8
Number of rotor teeth(--)	8
Number of parallel branches(--)	1
Number of turns per phase(--)	16
Number of turns per coil of field winding(--)	600
Rotor tooth width(°)	30/60
Number of field windings(--)	1
Armature winding effective length(mm)	240
Maximum air-gap length(mm)	34
Minimum air-gap length(mm)	2

A. Finite element model of EM

Fig. 16 shows the flux density distributions of EMs simulated by 3-D FEA corresponding to the HIMs with rotor tooth width $\pi/6$ and $\pi/3$. It can be found that the flux density generated by the field winding of EM is closed in the radial plane. Hence, the two-dimensional (2-D) models of them are adopted to simulate. The simulation 2-D models of the HIMs with different rotor tooth width $\theta_t = \pi/6$ and $\theta_t = \pi/3$ are shown in Figs. 17 and 18 respectively. The simulation circuit of WSM is shown in Fig. 19, where each phase of armature winding consists of three parts in series. Through this way, the

armature windings of Parts 1, 2 and 3 can be connected in series. The resistance R_{al} and leakage reluctance $l_{ls,end}$ of armature winding end are also considered in the circuit.

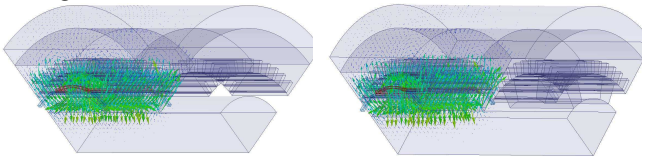

(a) (b)

Fig. 16. Magnetizing flux density of EM. (a) $\theta_t = \pi/6$. (b) $\theta_t = \pi/3$.

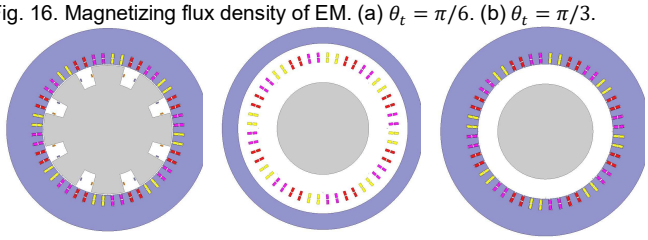

(a) (b) (c)

Fig. 17. 2-D FEA models of WSM when the rotor tooth width of HIM θ_t is $\pi/6$. (a) Part 1. (b) Part 2. (c) Part 3.

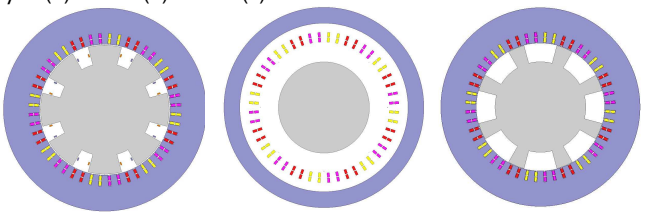

(a) (b) (c)

Fig. 18. 2-D FEA models of WSM when the rotor tooth width of HIM is $\pi/3$. (a) Part 1. (b) Part 2. (c) Part 3.

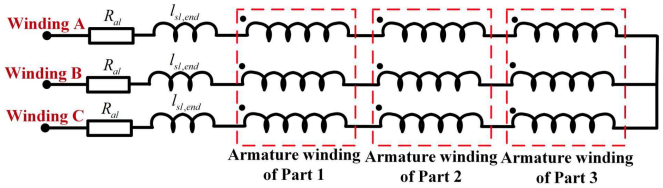

Fig. 19. Simulation circuit of EM.

B. Simulation

Case 1: $\theta_t = \pi/6$.

According to the analyses in Section IV, the rotor tooth width of Part 1 is $\pi/6$, and the rotor surfaces of Parts 2 and 3 are smooth. Meanwhile, the maximum and minimum air-gap lengths of Part 1 are 34 and 2 mm, and the air-gap length of other parts is 34 mm. The performances of HIM and EM under no-load condition predicted by FEA are compared. Fig. 20(a) shows the air-gap flux density distribution on both sides of field winding of HIM when the field current is 4 A. According to the analysis in Section IV, the field current of WSM is 3.72 A. Fig. 20(b) shows the flux lines of EM. The air-gap flux density waveforms obtained by spatial overlay and WSM are shown in Fig. 20(c), and it is shown that relatively good agreement is achieved. Fig. 20(d) shows the armature winding flux linkages of HIM and WSM under different excitation currents when the rotation speed is 2000 r/min. It can be found the flux linkages of HIM armature windings can be well predicted by the equivalent WSM.

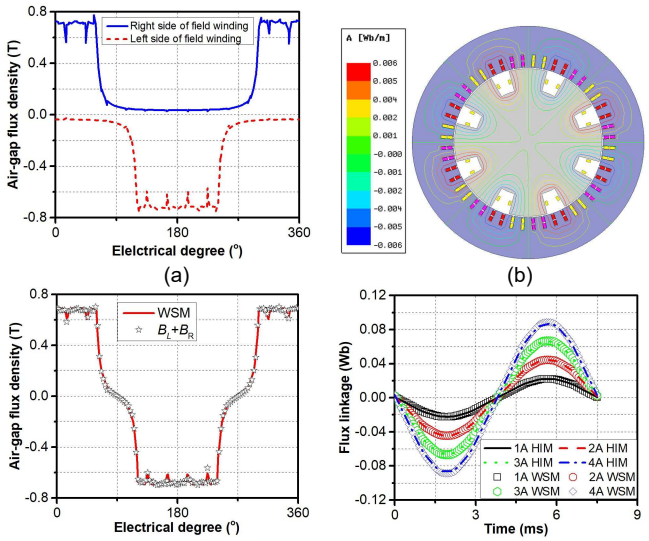

(a) (b) (c) (d)

Fig. 20. (a) Air-gap flux density of HIM on both sides of field winding. (b) Flux lines of EM. (c) Air-gap flux density of WSM and $B_L + B_R$, respectively. (d) Flux linkages of armature winding

Fig. 21 shows the self- and mutual inductances of armature windings when the field current is 4 A. The inductances of WSM are divided into four parts, including those of armature end winding, Parts 1, 2 and 3. The end winding inductance of armature winding can be obtained by the method in [25]. It can be seen that the self- and mutual inductances of Part 1 changes with rotor rotation, while those of the armature winding end, Parts 2 and 3 are constant. The inductances of Parts 2 and 3 can be seen as the end leakage inductances of EM. The average self-inductances of EM, Parts 1, 2, 3 and armature end winding are 230.1, 160.2, 47.8, 11.8 and 10.3 μH, respectively. The averages mutual inductances of EM, Parts 1, 2, 3 are -65.1, -55, -7.6, and -2.5 μH, respectively. It can be obtained that the leakage self-and mutual inductances of EM is 69.9 and -10.1 μH, which account for 30.37% and 15.51% of the total self- and mutual inductances, respectively. The frequencies of the self- and mutual inductance of EM are twice the electrical frequency of machine. Comparing the inductance waveforms presented in Fig. 21, it indicates that the results obtained by the EM agree well with those of HIM except for some errors, which may be caused by the follow two reasons. i) The end winding inductance $l_{sl,end}$ of EM is calculated by the analytical method in [25], which is an empirical formula, and thus there may be an error between results obtained by the analytical and FEA calculation. ii) The edge effect of the 3-D HIM cannot be considered in the 2-D EM simulation.

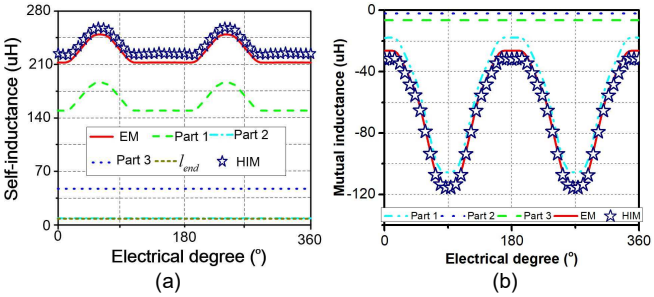

(a) (b)

Fig. 21. Inductance of armature winding. (a). Self-inductance.(b) Mutual

inductance.

To comparatively study the performances of EM and HIM on load state, the armature windings are connected to a three-phase symmetrical resistance load. One-fourth finite element (FE) model of HIM is used to save the computation time, as shown in Fig. 22, where Z_l is equal to 7.3 Ω and the output is ac terminal voltage U_l or current i_l .

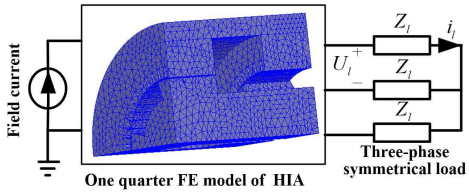

Fig. 22. Simulation model of HIM.

The output voltage waveforms of both EM and HIM are shown in Fig. 23(a). It can be found that the result of EM exhibits good consistency with that of HIM excepting some small deviation that occurs as results of the difference of FE mesh quality and the different degrees of the saturation of iron cores.

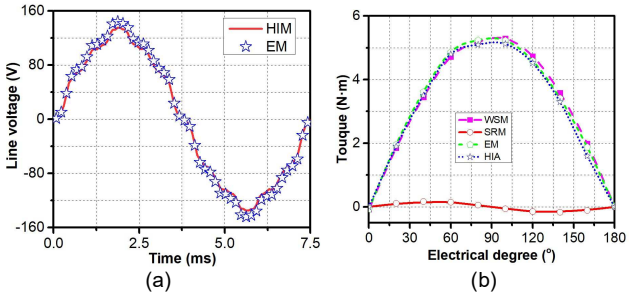

Fig. 23. (a) Output voltage waveforms of EM and HIM when $\theta_t = \pi/6$. (b) Output torque waveforms of EM and HIM when $\theta_t = \pi/3$.

Case 2: $\theta_t = \pi/3$.

According to the analyses in Section IV, the rotor tooth width of Parts 1 and 3 are $\pi/6$ and $\pi/12$ respectively, and the rotor surface of Part 2 is smooth. The maximum and minimum air-gap lengths of Part 1 are 34 and 2 mm respectively, and those of Part 3 are 34 and 1.03 mm respectively. Fig. 24(a) shows the air-gap flux density on both sides of HIM field winding. It can be found that the amplitudes of the left and right air-gap flux densities partially overlap under the same electrical angle, which makes the effective air-gap flux density obtained by spatial overlay method of this part being 0 T, as shown in Fig. 24(b). Compared with the air-gap flux density waveforms of the corresponding WSM, it can be seen that the two waveforms are consistent except for some errors which are caused by the edge effect of rotor tooth, as given in Fig. 24(c). Fig. 24(d) gives the flux linkages of HIM and corresponding EM under different exciting currents when the rotation speed is 2000 r/min, which indicates a good agreement between them. Meanwhile, the error caused by the edge effect has little influence on the flux linkages of the two models.

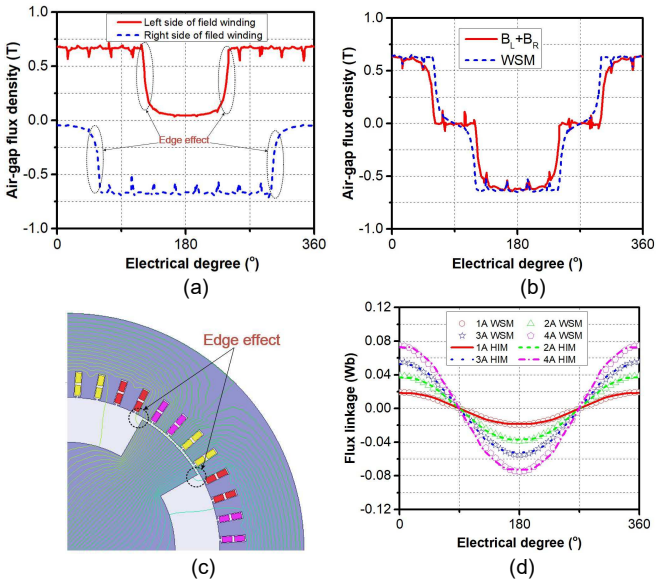

Fig. 24. Air-gap flux density of (a) HIM on both sides of field winding; (b) of WSM and $B_L + B_R$, respectively. (c) Edge effect diagram of HIM rotor. (d) Flux linkages of armature winding of EM and HIM when $\theta_t = \pi/3$.

The self- and mutual inductances of EM and HIM are respectively shown in Figs. 25 (a) and (b). Because of the rotor slots of the Parts 1 and 3, the self- and mutual inductances of their armature winding changes with the rotor rotation. Meanwhile, the inductances of Part 2 are constant due to the smooth rotor surface. The self- and mutual inductances of WSM are the sum of the self- and mutual inductances of Parts 1, 2, 3 and $l_{sl,end}$. Comparing the inductances of the HIM, it can be seen that the inductances of EM are agree well with those of the HIM.

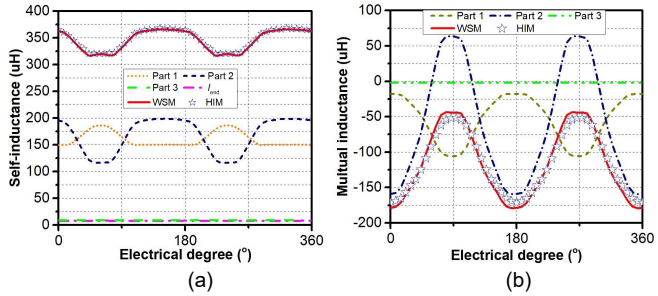

Fig. 25. Inductance of armature winding when the rotor tooth is π/3. (a). Self-inductance of armature winding.(b) Mutual inductance of armature winding.

To comparably study the load performances of the EM and HIM, the output torques of HIM and EM are investigated. The same three-phase symmetrical currents with the root mean square value 10 A are injected into the armature winding of two machines. The average output torques generated by the two machines under different initial phase of current are shown in Fig. 23(b). It can be found that the output torque of EM agrees well with that of HIM. Besides, the torque of the EM is generated by the WSM and SRM. While the average torque generated by SRM is much smaller than that of the WSM.

C. Experiment

Fig. 26 shows the structure of HIM with arc-shaped rotor tooth (the edges of the rotor teeth are arc-shaped). The EM

corresponding to this machine can be obtained by the aforementioned method. The flux density distribution of HIM with arc-shaped rotor tooth is almost the same with that of the HIM with radial rotor tooth, while the limiting speed of HIM with arc-shaped rotor tooth is relatively higher [23]. For good rotor dynamic performances, the topology of HIM with arc-shaped rotor tooth was chosen and its prototype with $\theta_t = \pi/6$ has been manufactured. Pictures of the stator, rotor and experimental platform are shown in Fig. 27 and the parameters of this machine are listed in Table I.

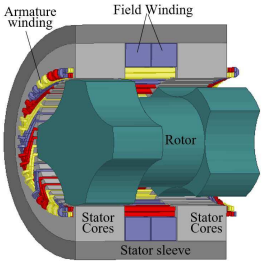

Fig. 26. Structure of HIM with arc-shaped rotor tooth.

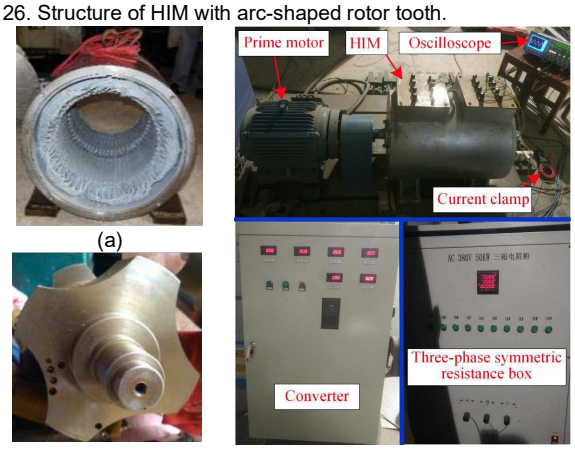

Fig. 27. Pictures of HIM. (a) Stator. (b) Rotor. (c) Experimental platform.

Figs. 28(a) and (b) show the measured phase back-EMF waveforms of HIM at 2000 r/min under open circuit state, where the field current is 0 and 5 A, respectively. It can be found that the phase back-EMF waveforms are approximately trapezoidal due to the shape of rotor tooth and the armature winding distribution. Besides, the amplitude of measured back-EMF is not 0 V when the field current is 0 A. It is caused by the iron core remanence of stator sleeve and rotor, which are made of 45# medium carbon steel. Fig. 28(c) shows the back-EMF waveforms of HIM and WSM obtained by FEA. The field current $I_{f,l}$ of EM is equal to $0.93I_f$. It can be found that the results obtained by FEA have the similar variation tendency with the measured results. Fig. 29(a) shows that the WSM predicted, 3-D FEA model of HIM predicted, and measured results of open circuit back-EMF under different exciting current when the rotation speed is 2000 r/min. Considering the influence of iron core remanence, the measured open circuit back-EMF curve is adjusted to obtain the open circuit characteristic curve of HIM [25]. The starting point of the curve is translated to the origin of the coordinate. It can be seen that the output voltage of EM and HIM obtained by FEA are in good agreement. In addition, it can be found that there are some inconsistencies between FEA and measured results, which may be caused by the leakage flux through the end caps of HIM, as shown in Fig. 29(b). To suppress the flux leakage, the end caps of the HIM are expected to be constructed by a non-magnetic material. However, in practice the end cap material of the prototype is not the ideal non-magnetic material and has weak permeability. Meanwhile, it is difficult to obtain the permeability curve of the material of end caps. Thus, the flux leakage though the end caps of HIM is hard to be considered in the simulation.

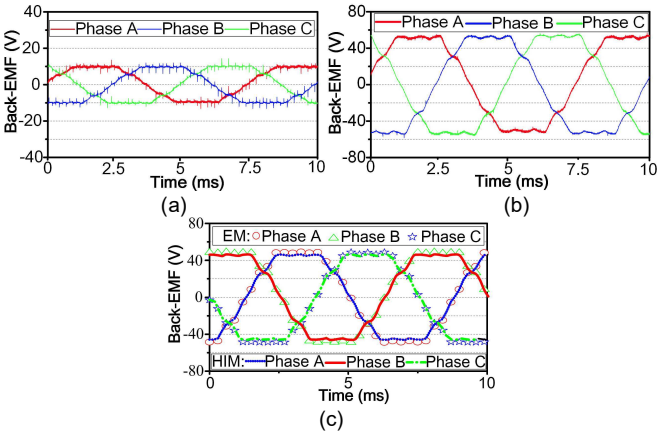

Fig. 28. The back-EMF waveforms at 2000 r/min. (a) Measured results when $I_f = 0$ A. (b) Measured results when $I_f = 5$ A.(c) Simulation results when $I_f = 5$ A and $I_{f,l} = 4.65$ A.

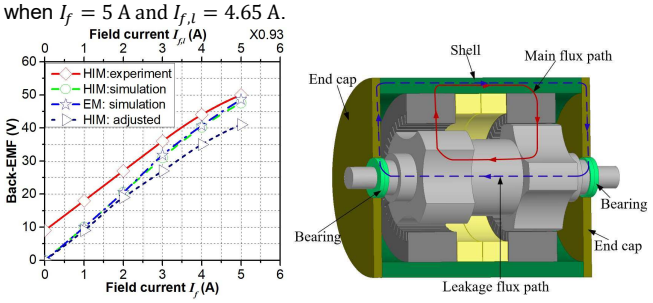

Fig. 29. (a) Variation of amplitude of phase back-EMF with field current at 2000 r/min. (The abscissa of "WSM: simulation" is $I_{f,l}$, others are I_f .). (b) Leakage flux path crossing the end caps.

Fig. 30(a) gives the experimental results of the phase current of HIM with different field current at 2000 r/min. It can be found that the phase current is not 0 A when the exciting current is 0 A, which is caused by the rotor and sleeve core remanence. Fig. 30(b) gives the comparison between the phase current amplitudes respectively obtained by experiment and FEA at different speeds when I_f is changed from 0 to 5 A and the resistance box has a resistance of 7.3 Ω per phase. It can be seen that the amplitudes of phase current of WSM and HIM obtained by simulation are matched well with each other. In addition, the results obtained by simulation are smaller than those of the experiment. The differences between simulation and experiment results become smaller with the increase of exciting current. The reason is that as the field current increases, the proportion of iron core remanence to the magnetic field of the entire motor will decrease. Though the results obtained by FEA is smaller than those of the measured, their variation trends are consistent, as shown in Fig. 31.

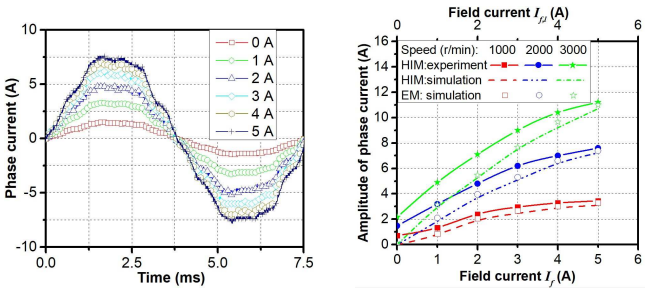

(a) (b)

Fig. 30. Load currents. (a) Experimental waveforms of the phase current of HIM with different field currents at 2000 r/min. (b) Variation of amplitude of phase current under different speeds and field currents. (The abscissa of "WSM: simulation" is $I_{f,l}$, others are I_f .)

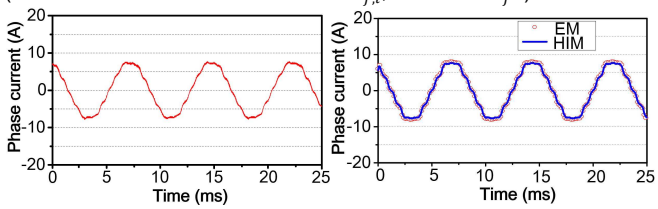

(a) (b)

Fig. 31. Load phase current waveforms at 2000 r/min when the exciting currents $I_f = 5$ A and $I_{f,l} = 4.65$ A. (a) Measured. (b) Simulation.

VI. Conclusion

The relationship between the HIM and the WSM has been established theoretically and validated in this paper. Firstly, the topology and basic operation principle of HIM are introduced. The mathematical expressions including the air-gap flux densities on both sides of the field winding, the back-EMF, the self and mutual inductances of armature windings, are derived. Based on these models and results, it is shown that the HIM can be regarded as a WSM with large end leakage inductance when rotor tooth width $\theta_t \leq \pi/\mathrm{p}$, or a combination of WSM and synchronous reluctance machine (SRM) when $\theta_t > \pi/p$.The relative values of the synchronous reactances x_d and x_q depend on the corresponding electric angle of rotor tooth width of HIM. When $\theta_t < \pi/4$, the synchronous reactances $x_d > x_q$; when $\theta_t = \pi/4, x_d = x_q$; and when $\theta_t > \pi/4, x_d < x_q$.Moreover, the air-gap flux density distributions, terminal voltages and inductances of WSM and HIM are comparatively investigated. It indicates that the results obtained by the equivalent machine agree well with those of the HIM. Finally, to verify the validity of the simulations and analyses, a prototype of HIM with arc-shaped rotor slot is tested. The results validate that the HIM can be regarded as a WSM or consisting of a WSM and a SRM, which should be helpful for the understanding, design and analysis of the HIM.

References

[1] V. Boicea, "Energy storage technologies: The past and the present," *Proc. IEEE*, vol. 102, no. 11, pp. 1777–1794, Nov. 2014.

[2] S. Vazquez, S. Lukic, E. Galvan, L. Franquelo, and J. Carrasco, "Energy storage systems for transport and grid applications," *IEEE Trans. Ind. Electron.*, vol. 57, no. 12, pp. 3881–3895, Dec. 2010.

[3] Arani, A. A. Khodadoost, et al. "Review of Flywheel Energy Storage Systems structures and applications in power systems and microgrids." *Renew. Sustain. Energy Rev.*, vol. 69, no. 6, pp. 9-18, Mar. 2017.

[4] T. D. Nguyen, K. J. Tseng, S. Zhang, and H. T. Nguyen, "A novel axial flux permanent-magnet machine for flywheel energy storage system: Design and analysis," *IEEE Trans. Ind. Electron.*,vol. 58, no. 9, pp. 3784–3794, Sep. 2011.

[5] I. Hadjipaschalis, A. Poullikkas, and V. Efthimiou, "Overview of current and future energy storage technologies for electric power applications," *Renew. Sustain. Energy Rev.*, vol. 13, no. 6, pp. 1513–1522, 2009.

[6] S.-M. Jang, J.-H. Park, D.-J. You, and S.-H. Choi, "Analysis on operational power and eddy current losses for applying coreless double-sided permanent magnet synchronous motor/generator to high-power flywheel energy storage system," *J. Appl. Phys.*, vol. 105, no. 7, pp. 07F116-1–07F116-3,Apr. 2009.

[7] J. Lahteenmaki, "Design and voltage supply of high-speed induction machines," Ph.D. dissertation, Helsinki Univ. Technol., Espoo, Finland, 2002.

[8] J. Pyrhonen, J. Nerg, P. Kurronen, and U. Lauber, "High-speed, high output, solid-rotor induction motor technology for gas compression," IEEE Trans. Ind. Electron., vol. 57, no. 1, pp. 272–280, Jan. 2010.

[9] J. F. Gieras and J. Saari, "Performance calculation for a high-speed solid-rotor induction motor," IEEE Trans. Ind. Electron., vol. 59, no. 6, pp. 2689–2700, Jun. 2012.

[10] W. L. Soong, G. B. Kliman, R. N. Johnson, R. A. White, and J. E. Miller, "Novel high-speed induction motor for a commercial centrifugal compressor," IEEE Trans. Ind. App., vol. 36, no. 3, pp. 706–713, May 2000.

[11] D. Gerada, A. Mebarki, N. L. Brown, C. Gerada, A. Cavagnino and A. Boglietti, "High-Speed Electrical Machines: Technologies, Trends, and Developments," IEEE Trans. on Ind. Electron. , vol. 61, no. 6, pp. 2946-2959, Jun. 2014.

[12] D. H. Lee, T. H. Pham, and J. W. Ahn, "Design and operation characteristics of four-two pole high speed SRM for torque ripple reduction," IEEE Trans. Ind. Electron., vol. 60, no. 9, pp. 3637–3643, Sep. 2013.

[13] P. Tsao, M. Senesky, and S.R. Sanders, "An integrated flywheel energy storage system with homopolar inductor motor/generator and highfrequency drive," *IEEE Trans. Ind. Appl.*, vol. 39, no. 6, pp. 1710–1725, Nov./Dec. 2003.

[14] C. Ye, J. Yang, X. Liang, F. Xiong, and W. Xu, " Investigation a high-frequency pulsed alternator integrated motor and alternator," *IEEE Trans. Ind. Electron.(early access)*

[15] E. Severson, R. Nilssen, T. Undeland, and N. Mohan, "Magnetic equivalent circuit modeling of the ac homopolar machine for flywheel energy storage," *IEEE Trans. Energy Convers.*, vol. 30，no. 4, pp. 1670–1678, Dec. 2015.

[16] Z. Lou, K. Yu, L. Wang, Z. Ren, and C. Ye, "Two-reaction theory of homopolar inductor alternator," *IEEE Trans. Energy Convers.*, vol. 25, no. 3, pp. 677–679, Sep. 2010.

[17] M. Siegl and E. A. Erdelyi, "Damper bars and their influence in operating homopolar inductor alternators for aerospace supplies—Part I: Determination of saturated time-dependent reactances," *IEEE Trans. Aerosp. Electron. Syst.*, vol. AES-9, no. 6, pp. 925–931, Nov. 1973.

[18] E. A. Erdelyi, "Influence of inverter loads on the airgap flux of aerospace homopolar alternators," *IEEE Trans. Aerosp.*, vol. AS-3, no. 2, pp. 7–11, Jun. 1965.

[19] L. Lorilla, "Investigation of the homopolar inductor alternator for automotive applications," M.S. thesis, Dept. Elect. Eng. Comput. Sci., Massachusetts Inst. Technol., Cambridge, MA, USA, 2000.

[20] G. Tajima, T. Kosaka, N. Matsui, K. Tonogi, N. Minoshima and T. Yoshida, "Control of wound field synchronous motor integrated with ZSI, " *in Proc. Int. Power Electron. Conf.*, 2014, pp. 2438–2444.

[21] Z. Lou, Y. Cheng, Y. He, Q. Shen, X. Xie and K. Yu, "Analytical Calculation of Synchronous Reactances of Homopolar Inductor Alternator," *IEEE Trans. Plasma Sci.*, vol. 43, no. 5, pp. 1462-1468, May 2015.

[22] E. Severson, R. Nilssen, T. Undeland and N. Mohan, "Analysis of the bearingless AC homopolar motor," *in Proc. 20th IEEE ICEM*, Sep. 2012, pp. 570–576.

[23] J. Yang, C. Ye, X. Liang, W. Xu, F. Xiong, Y. Xiang and W. Li, "Investigation of a two-dimensional analytical model of the homopolar inductor alternator," *IEEE Trans. on Appl. Supercond.*, vol. 28, no. 3, pp. 1-5, Apr. 2018.

[24] D. Gerada, A. Mebarki, N. L. Brown, C. Gerada, A. Cavagnino and A. Boglietti, "High-Speed Electrical Machines: Technologies, Trends, and

Developments," *IEEE Trans. on Ind. Electron.,* vol. 61, no. 6, pp. 2946-2959, Jun. 2014.
[25] T. A. Lipo, *Introduction to AC Machine Design*. Madison, WI: Wisconsin Power Electron. Res. Center, Univ. of Wisconsin, 1996.